



Observations of diffusion in the electron halo and strahl

Chris Gurgiolo¹ and Melvyn L. Goldstein²

¹Bitterroot Basic Research, Hamilton, Montana, USA

²Heliospheric Physics Laboratory, Code 672, NASA Goddard Space Flight Center, Greenbelt, MD, USA

Correspondence to: Chris Gurgiolo (chris@gurgiolo.com)

Received: 16 June 2016 – Revised: 24 October 2016 – Accepted: 9 November 2016 – Published: 15 December 2016

Abstract. Observations of the three-dimensional solar wind electron velocity distribution functions (VDF) using ϕ – θ plots often show a tongue of electrons that begins at the strahl and stretches toward a new population of electrons, termed the proto-halo, that exists near the projection of the magnetic field opposite that associated with the strahl. The energy range in which the tongue and proto-halo are observed forms a “diffusion zone”. The tongue first appears in energy generally near the lower-energy range of the strahl and in the absence of any clear core/halo signature. While the ϕ – θ plots give the appearance that the tongue and proto-halo are derived from the strahl, a close examination of their density suggests that their source is probably the upper-energy core/halo electrons which have been scattered by one or more processes into these populations.

Keywords. Interplanetary physics (solar wind plasma)

1 Introduction

The electron portion of the solar wind consists of four distinct populations: a thermal isotropic core (Feldman et al., 1975), a suprathermal halo (Feldman et al., 1975), a high-energy super-halo (Lin, 1998; Wang et al., 2012), and a field-aligned strahl (Rosenbauer et al., 1976, 1977). The general consensus is that the initial formation of the electron solar wind occurs in the corona through a combination of Coulomb collisions and wave–particle interactions (e.g., see Vocks et al., 2008; Vocks, 2012; Pavan et al., 2013; Che and Goldstein, 2014; Che et al., 2014) resulting in a core population and a beam-like suprathermal tail. The formation of the observed halo comes through a combination of Coulomb interactions of the beam-like suprathermal tail and either local whistler and/or kinetic Alfvén wave turbulence (Vocks et al., 2005). Che and Goldstein (2014) have suggested that the required

turbulence is generated from counterstreaming electrons produced in nanoflares. The strahl arises from the fraction of the beam-like suprathermal tail that is collisionless – those particles are strongly focused by the magnetic field into a beam propagating along the local field while the lower-energy core and halo move with the protons radially outward. Recently, Seough et al. (2015) have proposed that the strahl is formed directly from the halo via pitch-angle scattering. Simulations that do not include wave–particle interactions or turbulence have been run by Landi et al. (2012) with results closely matching observations. The simulations are run between 0.3 to 6.0 AU, well above the exosphere, and show the importance of Coulomb collisions. This does not, however, imply that wave–particle interactions and turbulence are unimportant as the simulations begin outside the corona, where it has been suggested that these processes will play a major role in determining the properties of the solar wind.

The first three of these populations moves radially away from the sun. There is significant overlap between the core and halo populations in velocity space, which makes it impossible to separate the two populations to obtain their individual characteristics without resorting to numerical fitting of the data to model electron velocity distribution functions (eVDFs) (for example, see Feldman et al., 1975; Maksimovic et al., 2005; Stverák et al., 2009). Changes in eVDF slope (average temperature) in the eVDF, however, indicate the existence of all three populations. The strahl flows along the background magnetic field (Rosenbauer et al., 1976, 1977) and is radial only when the magnetic field is radial. In the presence of nonradial magnetic field the strahl is often fully separable from the core/halo populations (see Fig. 5 in Gurgiolo et al., 2012) and the strahl moments can be computed by direct integration. At times, however, when the magnetic field has a significant radial component, the strahl will overlap the core/halo at one or more energies. If the strahl charac-

teristics are required during these times, then numerical fitting is necessary.

Interactions between interplanetary medium and the solar wind (especially the strahl) as it expands and propagates away from the sun are thought to be responsible for a number of observed effects. In the absence of collisions, focusing by the mirror force should narrow the strahl; however, in actuality the strahl is observed to broaden with radial distance from the sun (Pilipp et al., 1987a, b; Hammond et al., 1996). The broadening begins where pitch-angle scattering would be expected to dominate over focusing (~ 0.5 AU) (Owens et al., 2008). There are a number of sources of free energy in the solar wind (e.g., see Dum et al., 1980; Saito and Gary, 2007b, a; Gary and Saito, 2007; Gary et al., 2008; Viñas et al., 2010) available to drive the pitch-angle scattering. These include interactions of the strahl with sunward-propagating whistler waves (e.g., Vocks et al., 2008), scattering off of broadband whistler turbulence (Pierrard et al., 2011), and scattering by Langmuir waves (Pavan et al., 2013).

In addition to pitch-angle broadening of the strahl, Maksimovic et al. (2005) and Stverák et al. (2009) have shown that the strahl and halo densities vary in opposite directions with radial distances from the sun (the density of the strahl decreases in conjunction with an increase in the halo). This suggests that at least a portion of the strahl may be being degraded in energy and merged into the halo. The processes active in driving this are unknown, but it has been suggested that they include at least some of the same processes responsible for the broadening of the strahl. This is seen as a slow and continual erosion of the strahl and buildup of the halo through inelastic scattering.

Gurgiolo et al. (2012) have shown observations of what appears to be a strong local diffusion of the strahl in a restricted energy band where the strahl and halo overlap. This is an overlap in energy but not necessarily in the angular dimensions (of velocity space) and suggests that the buildup of the halo may not be a slow and steady process but may occur in “quantum” jumps within regions where the intense disruption of the lower edge of the strahl occurs. Any processes that may be involved in setting up the diffusion over and above those associated with pitch-angle broadening have yet to be identified.

In this paper we take a closer look at the diffusion signatures reported by Gurgiolo et al. (2012). Data from a number of different time intervals are looked at specifically in regard to how the diffusion signature varies with energy and the formation and characteristics of the proto-halo (a population of electrons that is formed in the diffusion zone) and the waves present within the regions where the diffusion is observed. Surprisingly, looking at the densities of the individual electron populations within the diffusion zone suggests that is not the strahl being disrupted as originally postulated by Gurgiolo et al. (2012) but the upper-energy halo electrons. It is the disruption of this population that apparently is the source of the electrons observed in the diffusion zone.

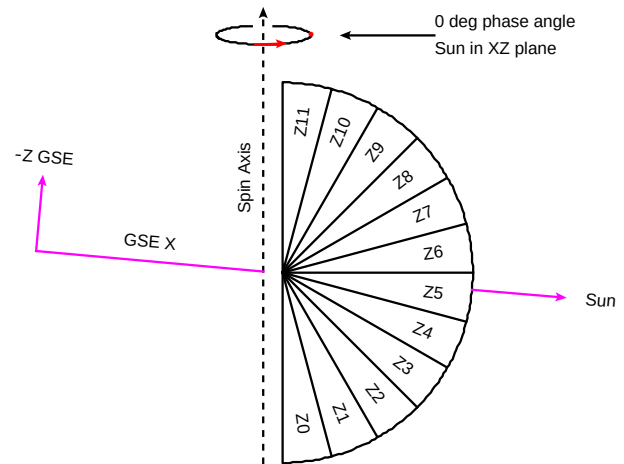


Figure 1. Schematic applicable to either of the two PEACE instrument heads showing the 12 elevation zones and their alignment in the PEACE frame of reference. The PEACE frame of reference is within 5° of GSE.

2 Data

This study uses data from multiple Cluster experiments, generally taken from the spacecraft with the cleanest data sets during the time being studied. The cleanest data are generally from either C1, which has the best proton data, or C2, which usually has the best electron data up to late May 2011 when there was a failure in the one of elevation zone sensors. We have restricted ourselves in this paper to time periods when the spacecraft were returning data using burst-mode telemetry. During those times the returned data are generally at or close to their highest resolution.

The electron data come from the Plasma Electron And Current Experiment (PEACE) (Johnstone et al., 1997; Frazier et al., 2010). Figure 1 shows a schematic applicable to either of the two PEACE heads, which are mounted 180° apart on the spacecraft body. The figure is drawn in the instrument frame of reference and for comparison includes the GSE Z and X axes. Each head consists of a fan of 12 elevation zones mounted parallel to the spacecraft spin axis. The spin axis is aligned to within 5° of $-Z$ GSE, which tilts the GSE ecliptic plane by -5° in the figure. The instrument uses the spacecraft spin to scan velocity space in azimuth. In the instrument frame of reference the 0° azimuth angle defines the location at which the fan of sensors is in the plane defined by the GSE XZ axes (the plane containing the sun). Most of the data in this study come from the low-energy electrostatic analyzer (LEEA) head, but there are some data intervals when the data come from the high-energy electrostatic analyzer (HEEA). The major difference between the two heads is that HEEA has a larger geometric factor.

We used combined full-resolution data from the fluxgate magnetometer (FGM) (Balogh et al., 1997; Gloag et al., 2010) and together with waveform magnetic field data from

Spatio-Temporal Analysis of Field Fluctuations (STAFF) (Cornilleau-Wehrlin et al., 1997, 2010) to produce magnetic field power spectra. Five vector per second FGM data are used to indicate the location of the projections of the magnetic field head and tail locations in all the ϕ - θ plots used in the paper.

The spacecraft potential data are used to correct the measured energy in moment estimates and were provided by the Electric Field and Waves (EFW) experiment (Gustafsson et al., 1997; Khotyaintsev et al., 2010).

In burst-mode telemetry PEACE returns a continuous set of full 3-D eVDFs with a time resolution of the spacecraft spin rate (~ 4 s). The energy and angular resolutions, however, are variable and depend on the instrument mode, but in general the data come from 32 azimuth sectors, 6 or 12 elevation sectors, and 30 or 60 energy steps. To obtain the highest resolution (time, energy, and angular) within the diffusion energy range, we used burst-mode data of all the analyses within this paper. In burst-mode telemetry the FGM full-resolution magnetic field data are generally sampled at 67 vectors per second and the STAFF waveform data at 450 vectors per second. This allows spectra to be computed through the ion scale length and down toward electron scales.

With the exception of PEACE data, which was obtained from the Mullard Space Science Laboratory (MSSL) science data archive, all data were obtained from the Cluster Science Archive (CSA, <http://www.cosmos.esa.int/web/csa>).

3 ϕ - θ plots

ϕ - θ plots are used throughout to illustrate features in the electron eVDFs. This mode of presentation allows one to show the entire three-dimensional distribution function at a given energy as a two-dimensional projection. We discuss its primary features and some caveats of which the general user should be aware.

A ϕ - θ plot shows data within a spherical shell in phase space associated with a single returned energy step. The data are plotted in the instrument frame of reference as a function of the instrument azimuth (x axis) and elevation (y axis) viewing angles. Elevation angles are measured from the spacecraft spin axis and azimuth angles are the spacecraft rotation angles, where an azimuth of 0° is the angle at which the instrument aperture is pointing toward the sun. Thus, (0° , 0°) represents approximately radial flow from the sun (but not exactly because the spacecraft spin axis is tilted by about 5° off of $-Z$ GSE). The location of the head and tail of the local magnetic field in each plot is shown as a circle and triangle, respectively. If the plot has been autoscaled, the scaling range is shown immediately above it. Also shown above the plot will be the center energy (raw and potential corrected) of the plotted data. The intensity in each plot is log-scaled.

Examples of the plot format are illustrated in Fig. 2, which shows two columns of five ϕ - θ plots. Both columns show

only a subset of the energy steps being returned. The starting time of the spin of data used in the plots is shown at the top of each column. The left-hand column of plots is a sequential set of cuts in energy through the solar wind eVDF. The energy range shown contains the upper-energy edge of the core/halo and the lower-energy edge of the strahl. The core and halo populations always overlap in a ϕ - θ plot and cannot be separated. They are treated as a single population called the core/halo and are centered in the plot and move anti-sunward. Because the strahl is field-aligned, it will always be centered on one of the two magnetic field points (in this case the head). Note that while the core/halo and strahl overlap in energy they are, in this example, fully separable in angle because there is a significant nonradial component of the magnetic field that shifts the strahl off the core/halo. The angular separation allows the two populations to be masked off and then integrated to provide for two separate sets of moments, one for the core/halo and one for the strahl.

The right-hand column of ϕ - θ plots is derived from a typical foreshock eVDF and shows characteristics similar to what is seen in the first column of plots with the exception that it contains a population of return electrons centered on the magnetic field tail projection point (moving sunward). These electrons are either solar wind electrons that have been scattered off the bow shock or electrons that have leaked through the bow shock from the magnetosheath. This population is present anytime a spacecraft is in the foreshock (Larson et al., 1996) and can be used to determine if the spacecraft is interior or exterior to the foreshock. It generally has a much higher thermal energy than does the strahl.

While ϕ - θ plots are extremely useful in looking at details of the eVDF, there are certain caveats one needs to keep in mind. These caveats arise both from the map projection used in displaying the data and from various preprocessing algorithms and will be briefly touched on below. First and foremost, however, one should recognize that the primary purpose of this plot format as applied to this paper is to highlight features of the eVDF that are relevant to the objectives of this analysis.

Map projection format. The plots in Fig. 2 are shown using a Cartesian map projection. The Cartesian projection tends to distort objects at extreme elevations (but it has the advantage over, say, spherical projections that the entire azimuthal range can be displayed at once). While this distortion is most obvious in populations near the poles, it is rarely severe enough to completely mask the population morphology. When it is, one can use an orthographic projection, which does not exhibit the distortion. However, because this projection only shows half the sphere and the viewing angle needs to be orientated to adequately show the features in the data to be highlighted, it is not particularly useful for scanning large stretches of data where shifts in the magnetic field need to be frequently taken into account. That aside, it

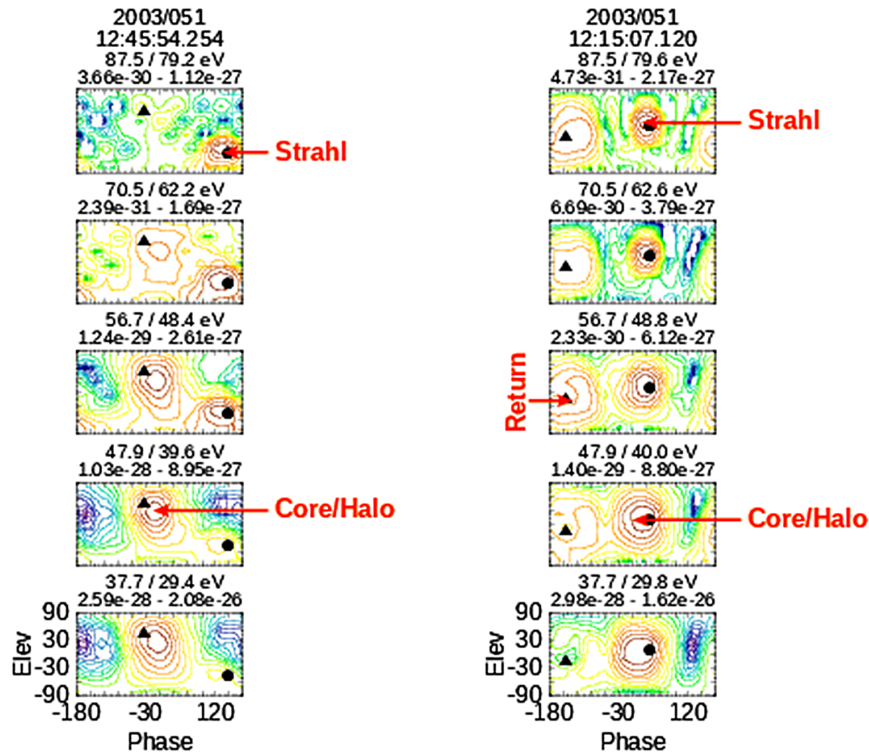


Figure 2. ϕ - θ plots from the solar wind (left) and the foreshock (right). The solar wind consists of a core, halo, and strahl population. The core/halo appear as a single population in the plots, but because of the energy range covered, it is probably primarily the halo that is seen. The foreshock is identical to the solar wind but includes a set of return electrons that are moving back upstream.

is possible to plot the ϕ - θ plots in a large number of mapping projections. The left column of plots in Fig. 3 shows the identical set of plots in the right-hand column in Fig. 2 but plotted using a cylindrical equidistance mapping projection.

Magnetic field projection points. Variations in the magnetic field within the time covered by a 3-D eVDF can affect the position of the projection points with respect to features in the eVDF, leading to possible confusion. For this reason the magnetic field used generally has a higher temporal resolution than the eVDF. The magnetic field vectors accumulated within the time interval associated with the 3-D eVDF can either be simple averages with the averaged values used to form the projection points, or all of the project points formed from the individual magnetic field vectors can be shown in the ϕ - θ plots. The first usage allows for a very exact estimation of the magnetic field within the time covered by a ϕ - θ plot while the latter (shown in the right-hand column of plots in Fig. 3) is often used when it is suspected that the magnetic field has significant variation within the plot time. In this case (from the figure) the magnetic field is seen to have enough jitter to broaden the two projection points but not enough to significantly

cause any confusion of the location of the projections with respect to strahl.

Smoothing. It is standard practice when producing ϕ - θ plots to subject the data to a spherical harmonic analysis as a means of smoothing the eVDF (Viñas and Gurgiolo, 2009). This in essence artificially increases the total density of data points in the plot. The advantage of using spherical harmonics is that they smooth without creating spurious new features. The left-hand column of plots in Fig. 4 shows the identical plots in the left-hand column of Fig. 2 but with no smoothing and contouring turned off. The individual colored grids match the instrument angular resolutions. The plots are definitely coarser than those shown in Fig. 2, but the same features are seen in both. This is not surprising. Viñas and Gurgiolo (2009) have shown that the plasma moments formed during a spherical harmonics analysis are virtually identical to those formed from the raw data, implying that the fitting to a set of spherical harmonics has minimal effect on the actual eVDFs.

Scaling. In general individual ϕ - θ plots are autoscaled. To intercompare plots within a column of plots, the autoscaling should be turned off. The right-hand plots in Fig. 4 show the same plots as in the left-hand column

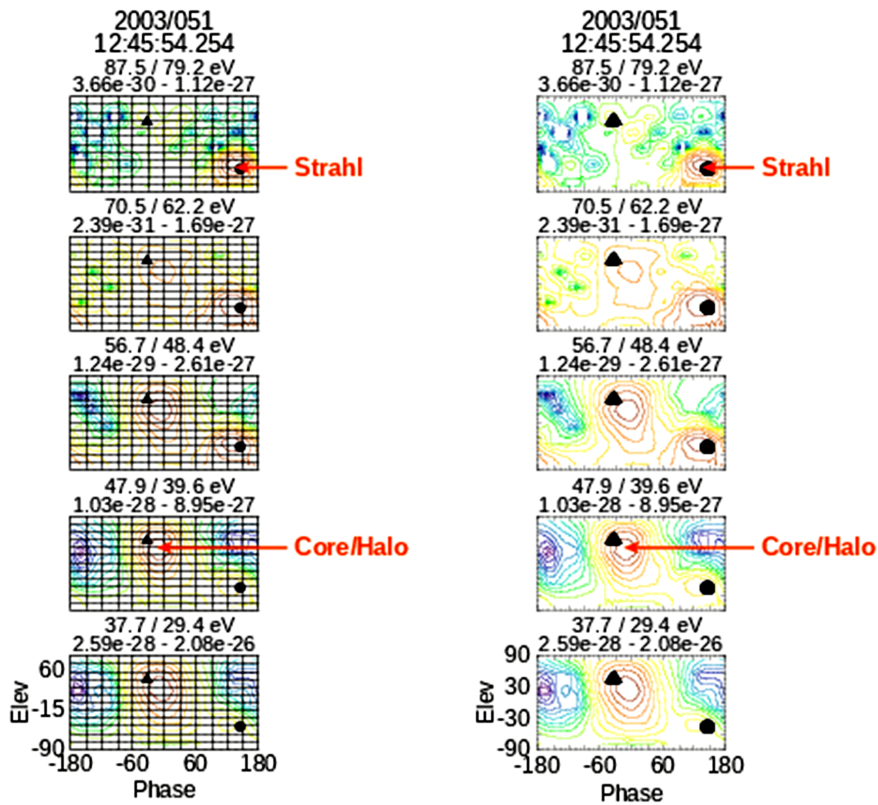


Figure 3. ϕ - θ plots identical to those on the left in Fig. 2. Here the left-hand column of plots shown is a cylindrical equidistance projection and the right column of plots is shown using the full-resolution magnetic field projection points (about 20 values).

of Fig. 2 but with autoscaling turned off. In this case the scaling used in all plots is given by the color bar at the bottom of the column. Autoscaling is useful when the column of plots spans a large energy range where there is enough fall-off in intensity that features in the high-energy plots are lost due to an insufficient number of contours and/or colors.

As noted above when the magnetic field has a large non-radial component, as in the solar wind example in Fig. 2, the core/halo can be fully separated due to the offset of the strahl from the core/halo. Even when there is a strong radial component in the field as in the foreshock example in Fig. 2, it is still possible to estimate the approximate transition energy where the plasma is shown in the ϕ - θ plots transitions from primarily strahl to the core/halo even though the two populations cannot be fully separated. Note that near 47.9 eV there is a small but noticeable shift in the overall distribution from a slightly off-radial to a more radial flow. This is the energy at which the core/halo becomes the more dominant population.

4 Observations

Between 2001 and 2012 inclusive, there were over 180 time intervals when the Cluster spacecraft were partially or totally

upstream of the bow shock (in the solar wind and/or foreshock) and the spacecraft were using burst-mode telemetry. The periods vary between 1.5 to 4 h in length and are generally made up of a mixture of pure solar wind and foreshock plasma. Seventeen of these periods were identified as containing definite diffusion signatures. The identifications were made using restrictive criteria that required eVDFs to exhibit both a tongue of electrons that extends from the strahl towards the opposite magnetic field projection point and a clear observation of a proto-halo population in one or more energy steps. There were a number of other times during which only a tongue of particles was seen with no distinct proto-halo population. In those cases, either the proto-halo did not form or was too weak to be observed as a clear and distinct particle population within the tongue. These events are not included in this study.

It should be noted that it is entirely possible that the tongue of particles associated with diffusion observations might be the result of the overlap in velocity space of one or more of the core/halo, strahl, and proto-halo populations. In this case the appearance of the tongue is controlled by the individual densities and temperatures of the populations involved and the tongue would not be an independent population. There are reasons to believe that, at least in many observations, the tongue is a population of particles formed in the dispersion.

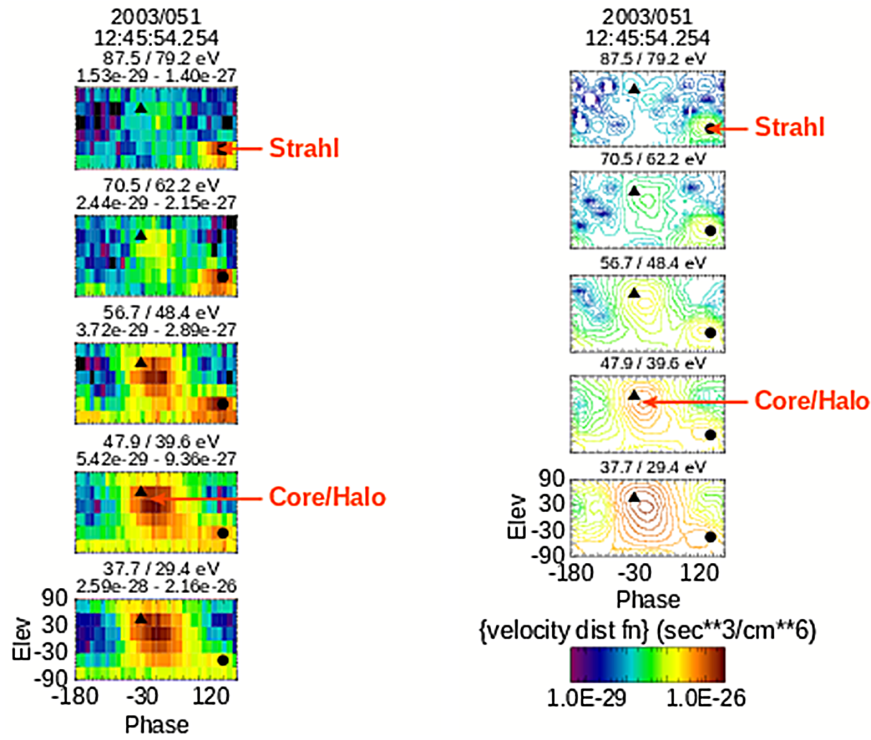


Figure 4. ϕ - θ plots identical to those on the left in Fig. 2. Here the left-hand column is plotted without any smoothing or fitting and the right column of plots is shown with autoscaling off. In this case all plots have identical scaling according to the color bar at the bottom of the column.

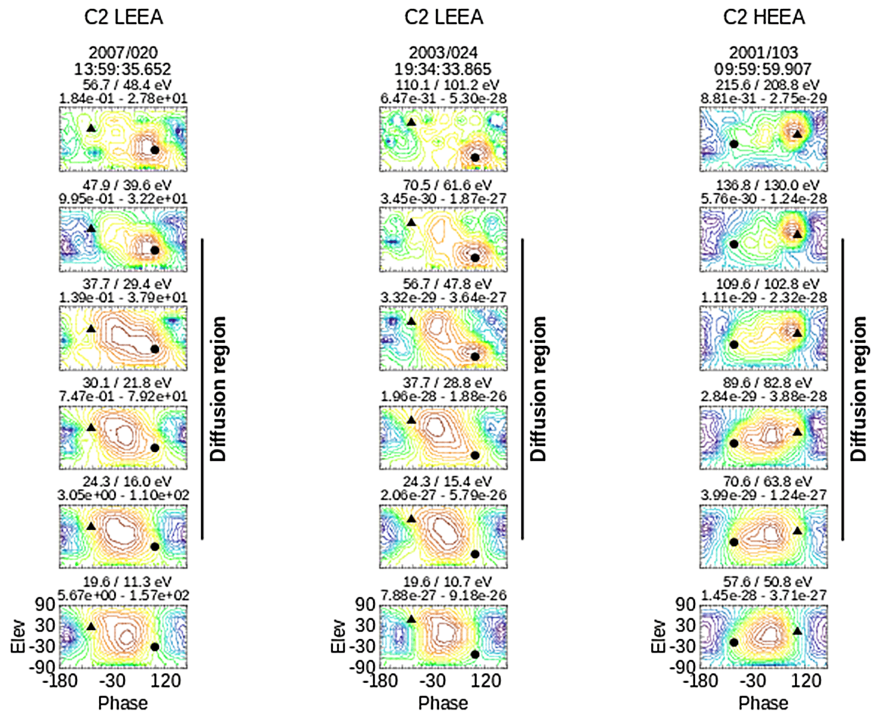


Figure 5. Three sets of ϕ - θ plots showing dispersion signatures within three eVDFs. The three sets of plots are each from a different time period.

Consider the left-hand column of plots in Fig. 2 which show a partial eVDF typical of the pure solar wind containing a core/halo and strahl population. There is no evidence of a tongue at any of the energy steps where both populations are observed. Contrast this with the left-hand column of plots in Fig. 9, which shows a subset of energies from a single eVDF within a region of diffusion. Here the tongue appears to develop, with the emergence of the proto-halo suggesting some connection between the two, which would make sense if the proto-halo is in essence a reformation of the strahl. Still, this cannot be proven conclusively with the data available but maybe with future modeling.

The diffusion signatures in each of the included 17 cases are similar in appearance. The major differences are the energy ranges over which the diffusion was observed and the direction of the tongue, the latter depending on the orientation of the magnetic field. Figure 5 contains three examples of diffusion from different times in different years. Each column of plots is a partial representation of a single eVDF. The vertical bar to the right of each column is the energy range in the eVDF that comprises the diffusion zone, extending from the upper energy where the electron tongue first appears down to the energy at which the proto-halo is no longer observable. The energy steps in the first column of plots are contiguous but are not in the next two columns of plots. The ϕ - θ plots at the upper- and lower-energy limits of the diffusion zone, however, are included. The three examples detail not only the effect of magnetic field orientation on the diffusion (orientation of the tongue) but also variations in the energy range of the diffusion zone. Figure 6 shows the identical set of plots as the right-hand column of Fig. 5 but with both smoothing and contours turned off. The plots in the figure reinforce the claim that smoothing does not significantly alter features in the eVDFs but simply makes them easier to pick out.

The characteristics associated with diffusion observations are presented and discussed here in the context of a 48 min stretch of data from 6 April 2008 (DOY 97) between 05:55 and 06:43 UT from the Cluster-2 LEEA analyzer, which was returning data in 12 elevation bins, 32 azimuth bins and 30 energy steps covering 7 to 3952 eV. During this time interval the spacecraft was in the vicinity of the bow shock/magnetosheath with multiple transitions into and out of the foreshock and pure solar wind. Diffusion signatures were seen in each solar wind interval. This is a period of fast wind with an average wind speed of over 700 km s^{-1} .

Figure 7 shows a set of spectrograms covering the time period from the two PEACE elevation zones closest to the ecliptic plane. The plot begins at the onset of the burst-mode telemetry and runs until the spacecraft begins making multiple short excursions into and out of the magnetosheath. The lines in the top plot indicate times when the spacecraft was in pure solar wind. Those intervals are coincident with noticeable depressions in the intensity of the $> 80 \text{ eV}$ electron fluxes that result from the absence of return electrons. This

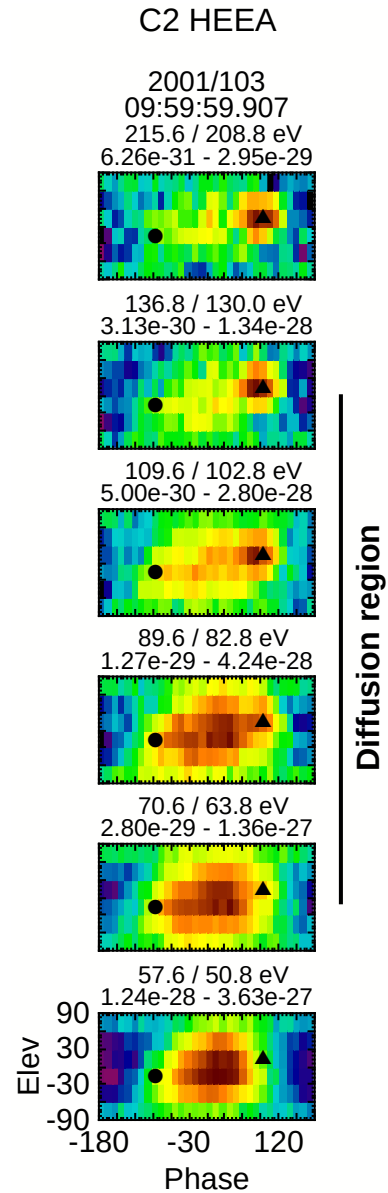


Figure 6. Five ϕ - θ plots identical to the right-most column of plots in Fig. 5 with no smoothing or contouring. The figure reinforces the claim that smoothing neither alters nor adds any features that exist in the eVDF. The tongue and proto-halo are both clearly seen in the plots.

is an adequate but not always sufficient indicator of being in pure solar wind. A better indicator is the total electron temperature as seen in Fig. 8 together with the full electron density, speed, and the magnetic field components for the time interval plotted in Fig. 7. As is readily seen in the figure, the electron temperature hits a baseline value whenever the spacecraft is in the solar wind. The inclusion of the higher temperature return electrons in the foreshock lifts the temperature off that baseline.

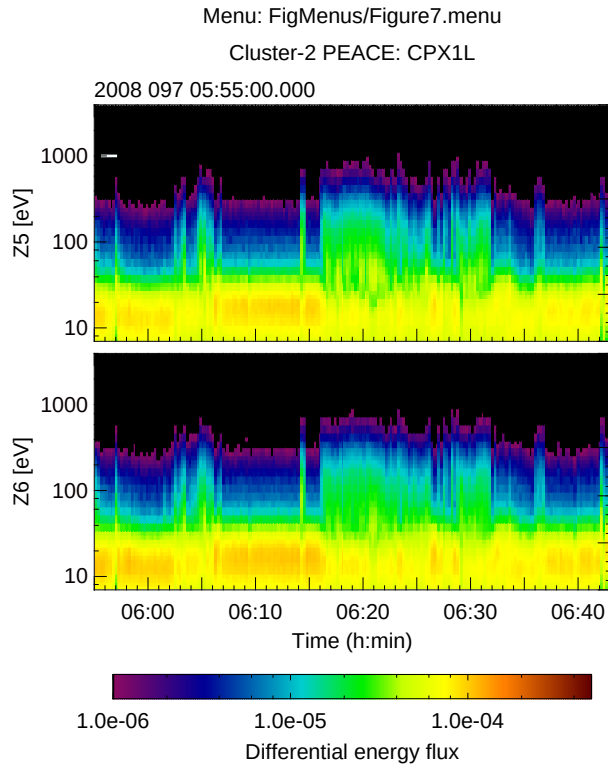


Figure 7. Spectrograms of the PEACE elevation zones above and below the ecliptic plane. The interval shown includes multiple excursions into and out of the solar wind and foreshock. Arrows show depressions in the intensity, which are intervals where the spacecraft was in the solar wind and in the presence of diffusion. The intensity depressions are the result of the absence of return electrons.

The observed diffusion during this time period is consistent and strong. A good picture of its features is seen in Fig. 9. Shown are two sets of ϕ - θ plots generated from a single eVDF observed in a diffusion event. The left set of plots shows a contiguous set of energies covering the diffusion zone (~ 56.7 down to ~ 30.1 eV). The right set of plots shows energies above the diffusion zone with the lower two energy steps being contiguous with those in the left-hand set of plots. Above that every other energy step is shown. Features of interest are indicated by arrows and labels. At 70 eV and above one sees only the strahl population, which extends up to 584 eV (an energy step not included in the figure). The ϕ - θ plot at 669 eV is basically noise that appears significant only because of the autoscaling of the plot intensity. The formation of the tongue begins at about 56.7 eV and extends downward in energy to just about where the core/halo begins to emerge in the plots. At these energies both the proto-halo and strahl (where it exists) are embedded in the tongue. By 37.7 eV the strahl has weakened to the point where it is only minimally present. There also might be a minimal manifestation of the core/halo present at this energy; however, by 30.1 eV there is a strong core/halo population signa-

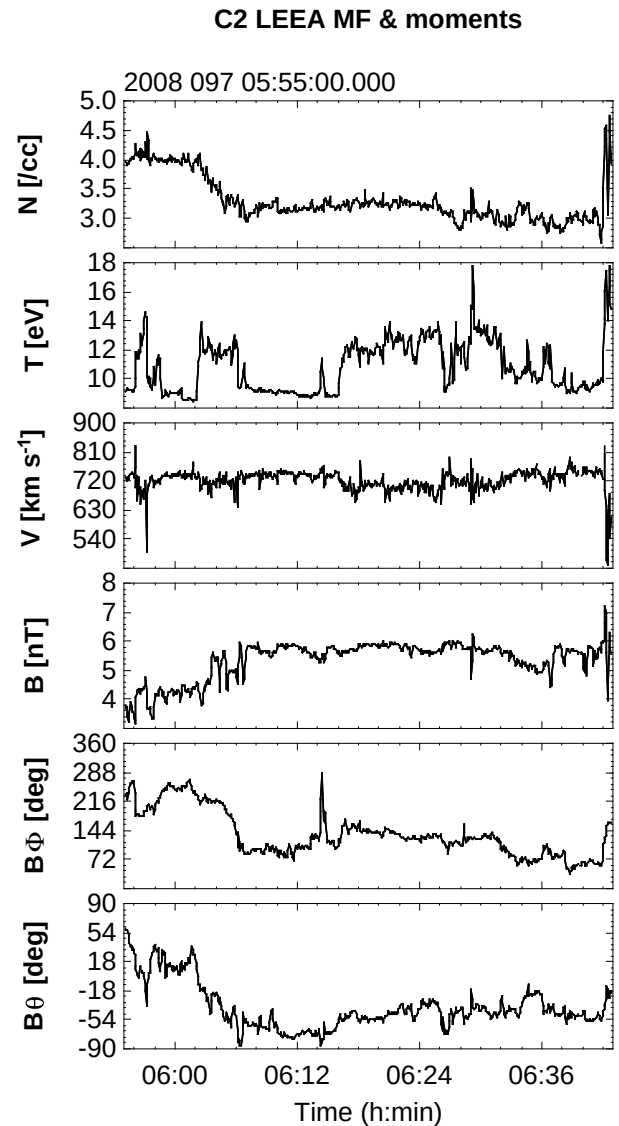


Figure 8. Plots of the total electron density, temperature, and speed and magnetic field components across the time interval in Fig. 7. The baseline temperatures occur when the spacecraft is in the solar wind. The inclusion of the higher temperature return population in the foreshock results in an increase in temperature above the baseline.

ture together with a proto-halo. Finally, at 24.3 eV only the core/halo population exists. It is reasonable to assume that the strahl covers the same energy range here as it would if there were no diffusion present; that is, the low-energy portion of the strahl is intact and has undergone no, or only minimal, diffusion. We will look at this in more depth when we discuss the density spectra within the diffusion region shown in Fig. 12.

There are two additional features of interest in the figure. At the higher energies the strahl is approximately centered on the magnetic field; however, at energies closer to the dif-

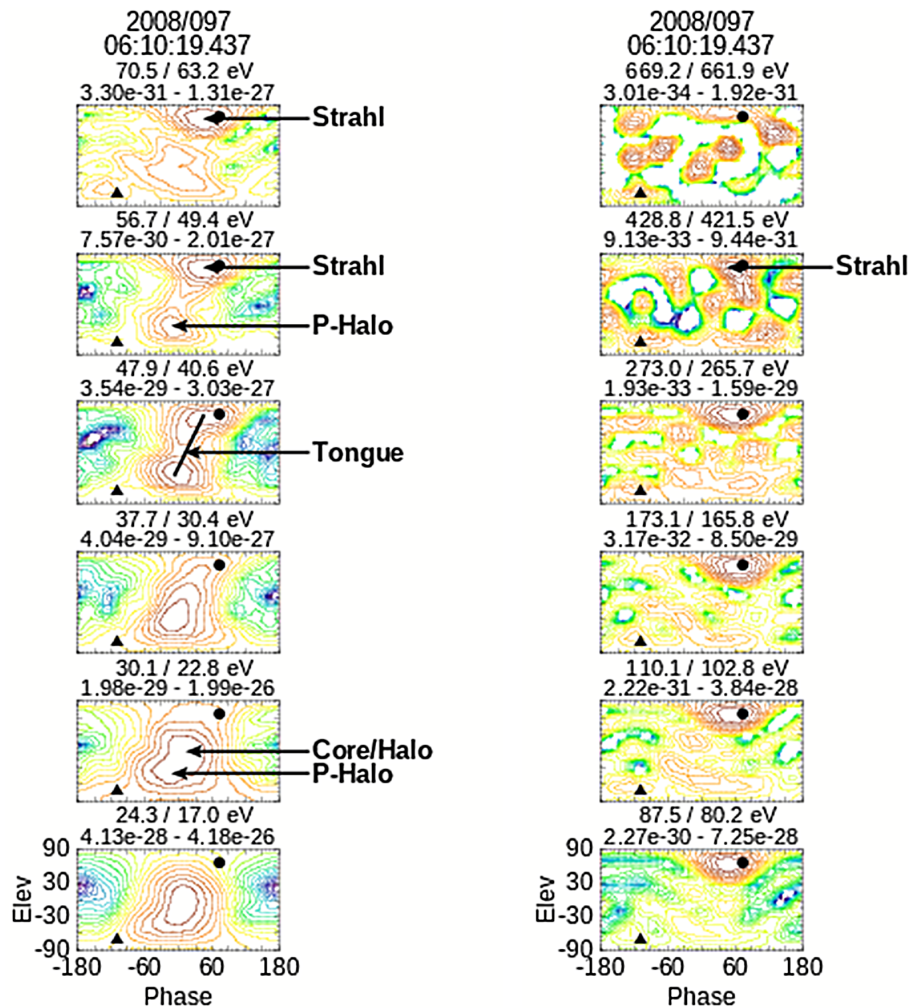


Figure 9. A set of ϕ - θ plots showing the formation of the tongue of electrons and the proto-halo as a function of energy. The left column shows continuous energy steps bracketing the diffusion, while the right column shows energies above the diffusion energy range. The two lowest energy steps in the right panel are a continuation of those in the left panel, while the remaining show every other energy step.

fusion zone the strahl shifts off the magnetic field. This shift is seen in almost every examined time period in which diffusion is present, but it is not seen, at least to the same extent, if at all, either in the solar wind in the absence of diffusion or in the foreshock. The second feature to note is the clear elliptical appearance of the strahl in and near the diffusion zone rather than the expected more circular appearance as seen in the foreshock eVDF in the right column of plots in Fig. 2. Both of these features seem to be unique to the diffusion process and may be the result of the mechanisms driving it.

Because the proto-halo and strahl are well separated in velocity space within this time period, it is possible within the energy steps where both populations exist to define velocity space volumes that individually isolate the two populations. Integrating over the volumes provides estimates of the density and velocity in each population. An example is shown in Fig. 10 for multiple eVDFs between 06:10:20 and

06:10:52 UT. Also included is a volume covering the tongue – the short region between the proto-halo and strahl. All the volumes are anchored to the projections of the magnetic field and will shift position in response to changes in field direction (and corresponding changes in the locations of the proto-halo and strahl). This generally produces stable long-term coverage of the populations but tends to break down when there are large-scale rotations in the field. The moments computed using the volumes are plotted in Fig. 11 between 06:08:00 and 06:12:00 UT for just the 47.9 eV energy shell where the proto-halo and strahl have comparable intensities. The panels in the figure from top to bottom show the density and normalized speed and fluid velocity components. These illustrate the general diffusion characteristics at the time of the plot, albeit in a single energy shell. Blue, red, green, and black traces represent the strahl, proto-halo, tongue, and total electron populations. The total density includes not only

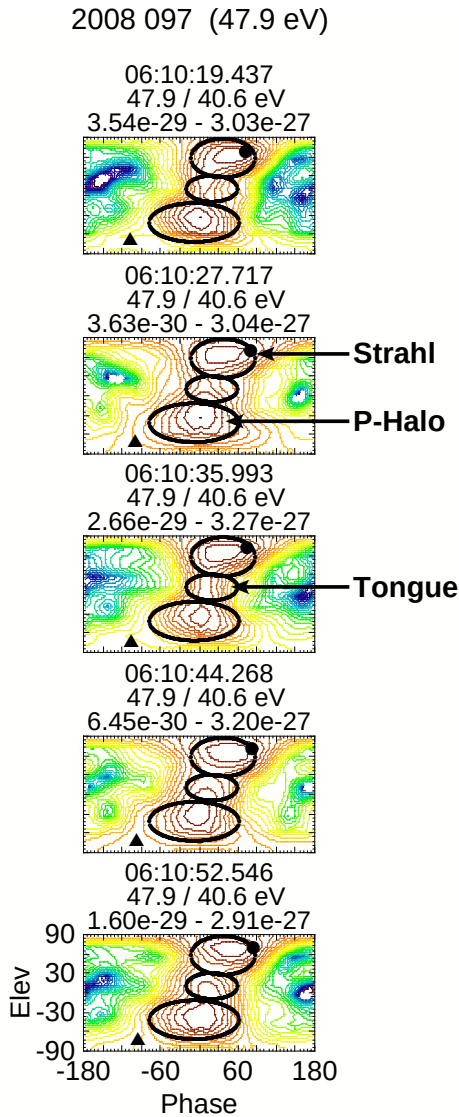


Figure 10. Five ϕ - θ plots of the 47.9 eV energy channel taken from different eVDFs within the time frame covered in Fig. 11 showing the volumes used to estimate the strahl, proto-halo, and tongue moments.

the individual population densities, but also any density exterior to the defined volumes. The normalized velocity is the contribution to the total velocity by a given population and is defined as

$$V_{P,n,i} = \frac{N_P}{N_F} V_{P,i}, \quad (1)$$

where the subscript i represents the velocity components (x , y , z), P is the population, and N_F is the full electron density.

The features seen in Fig. 11 are common to all the diffusion events looked at so far. The tongue contributes very little to either the density or to the total velocity. Both the strahl and proto-halo are moving basically anti-sunward (GSE V_x components are negative). The V_y and V_z components, how-

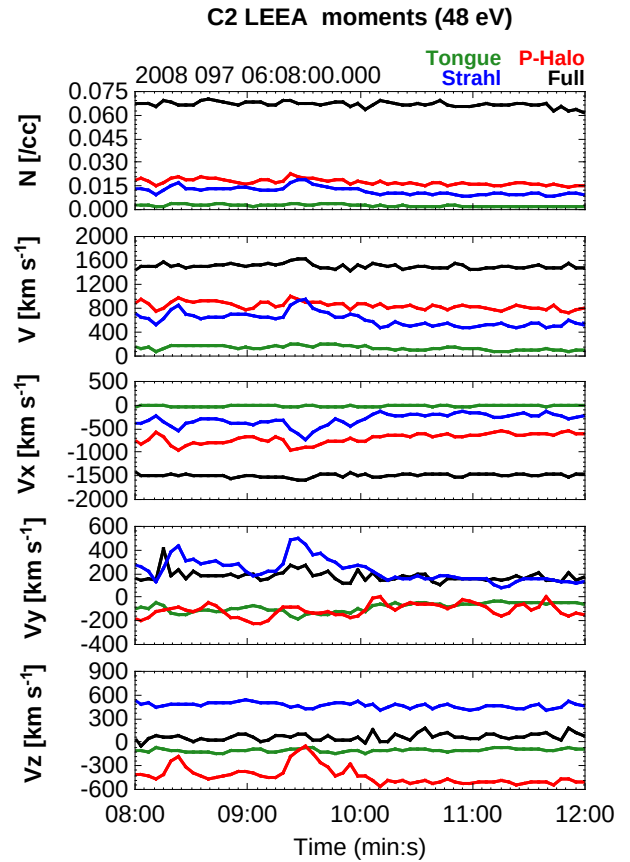


Figure 11. Electron plasma density, speed, and velocity (top to bottom) computed from the 48 eV energy channel. The moments are computed over the entire energy step (black), within the volume defining the proto-halo (red) and within the volume defining the strahl (blue).

ever, have close to opposite flows so that both the total V_y and V_z velocities are close to 0. This is true more for V_z and V_y . Basically, the overall flow at this energy step is approximately radial with an average energy in this energy channel ~ 7.3 eV, well below the measurement energy. Individually the average energy of each population is about 40 eV, consistent with the potential reduced measurement energy.

Figure 12 shows a pair of density spectra (the average density as a function of energy) over the energy range of 12.4 to 273 eV. The energy axis shows the instrument energy and not the potential corrected energy. These are equivalent to plots of the 1-D reduced eVDF. The top plot covers the time period in Fig. 11, where a strong diffusion signature is present, while the bottom plot covers a time when the spacecraft was in the solar wind with no visible diffusion signature. Black dots are the full density at each energy step, and the red dots are the strahl density within each energy step. The strahl density was not computed for the time shown in the bottom plot, and in the top plot the strahl density is computed only down to 48 eV. Below that, the strahl is no longer a distinct popu-

lation (cf. the 37.7 eV energy step in Fig. 9). The orange and purple lines are fits to the data above 60 eV for the full and strahl densities spectra, respectively. The difference in the intensity between the strahl and full-density spectra is due to the inclusion of the electrons outside the defined strahl velocity space volume. The shaded areas at the left in both plots show the mixture of populations present in the ϕ - θ plots. The diffusion zone is defined by the combined green, blue, and purple shadings in the top plot. This is a good picture of the general progression of electron populations within the diffusion zone and representative of the events we have looked at.

The top and bottom spectral plots are very similar in shape; this is despite the presence (absence) of diffusion in the upper (lower) plot, something to consider when using fits to model distributions to estimate the characteristics of the electron populations. Note that the data used to construct the bottom plot were taken approximately 2 years prior to the data used in the upper plot, so there should be no expectation for the spectral intensity in the two spectra to be comparable. Both full-density spectral plots show a break at 60 eV. In the top plot this corresponds to the energy where the tongue and proto-halo are first seen and in the bottom plot where the core/halo is first seen. The fact that there is no corresponding break in the strahl density spectrum suggests that the strahl plays no role in the break in the full-density spectrum.

We have also looked at the magnetic field spectral power in the absence and presence of diffusion. Two examples are shown in Fig. 13, taken during the times represented by the two density spectra in Fig. 12. Both are from pure solar wind, but the upper spectrum is from the time during which there was active diffusion and the lower from the time with no diffusion. Each spectrum is a combination of spectra built from the full-resolution FGM data (blue portion of the total spectrum) and the STAFF waveform data (orange portion of the spectrum), and both are normalized using their overlap between 1 and 2 Hz. The two spectra are very similar in the STAFF frequency range but show significant differences in the FGM portion. The FGM portion of the spectra is generally very dynamic even within adjoining time intervals. This carries through to the majority of the spectra generated in conjunction with this study. Both spectra are also very different from the typical spectra seen in the foreshock, an example of which is shown in Fig. 14. Foreshock spectra are overall flatter and tend to show broadband intensity enhancements in the STAFF portion of the spectrum (between 10 and 100 Hz in this figure). These enhancements are more than likely evidence of whistler or other broadband turbulence driven by the free energy in the counterstreaming return and strahl electron populations in the foreshock. It is interesting to note that there are generally no corresponding enhancements seen in the spectra during diffusion events, which probably precludes broadband turbulence as a source of the diffusion.

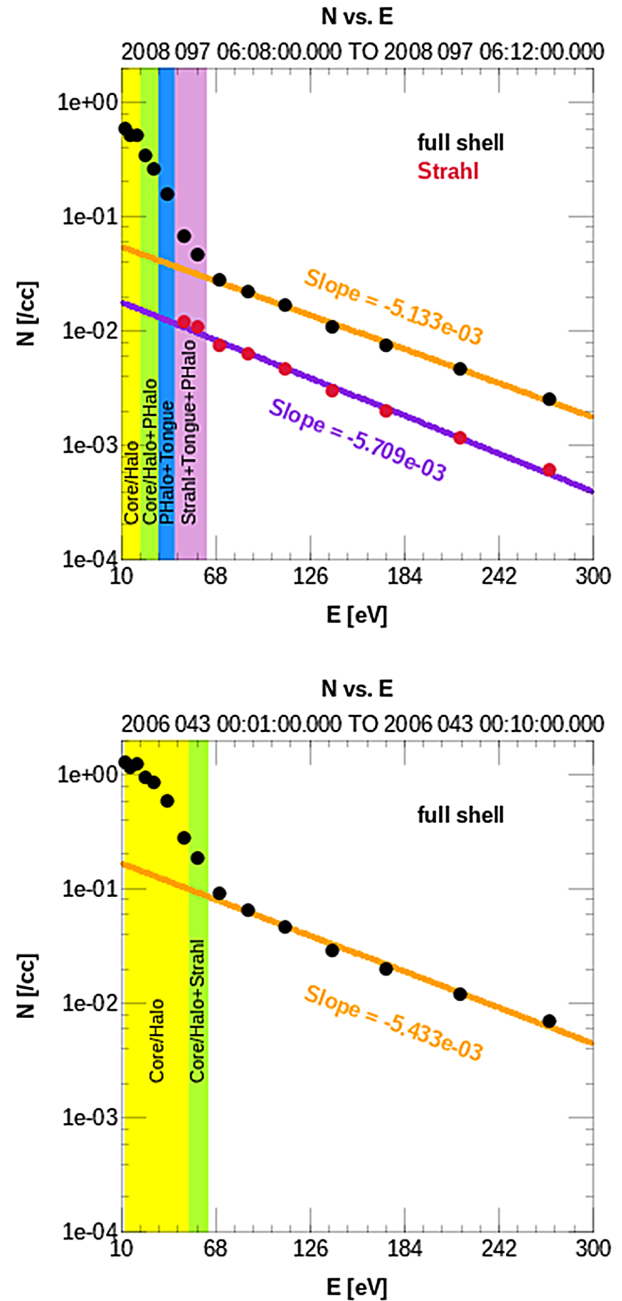


Figure 12. Density vs. energy curves computed for each of the 14 energy shells between 12.5 and 273 eV. The top figure is the average for the time period shown in Fig. 11. Black dots and red dots show the total density and strahl density in each shell. The strahl only covers the range where the population is visible. The bottom plot (showing only the total density) was taken from a 9 min period in the solar wind where there was no diffusion.

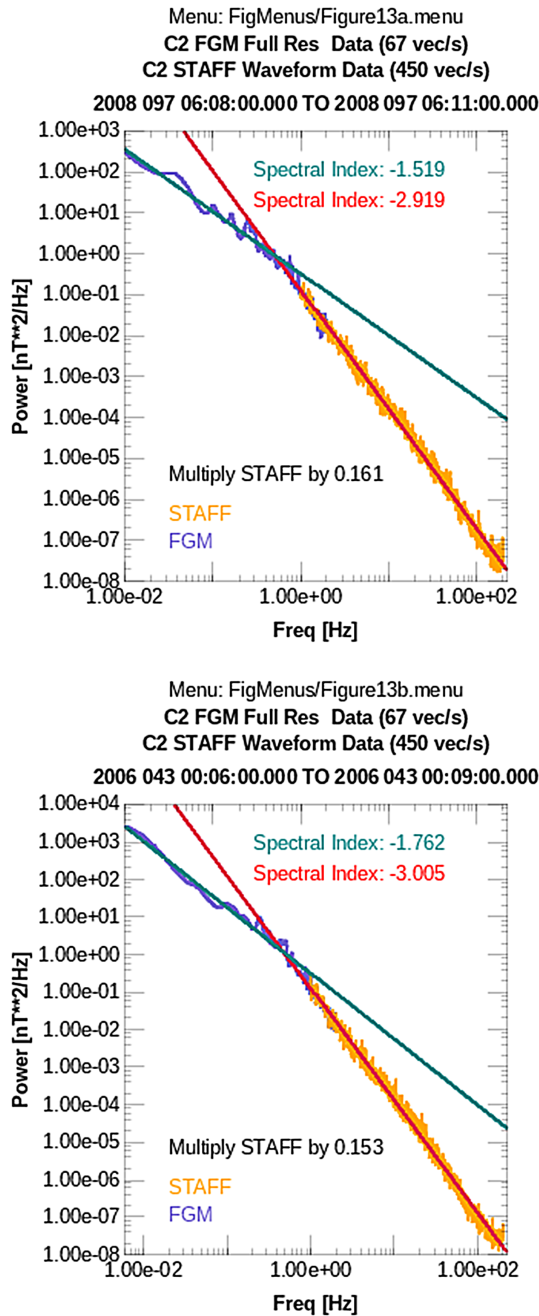


Figure 13. Magnetic field power density spectra during the two time periods used to form the N vs. E plots in Fig. 12. The spectra are formed from spectra using the full-resolution FGM data (blue portion of the spectra) and the STAFF waveform data (orange portion of the spectra). The two spectra are normalized between 1 and 2 Hz.

5 Discussion

Of the more than 180 intervals looked at when the Cluster spacecraft were upstream of the bow shock and returning data in burst-mode telemetry, almost 10% exhibit diffusion signatures that fit the restrictive definition given at the start

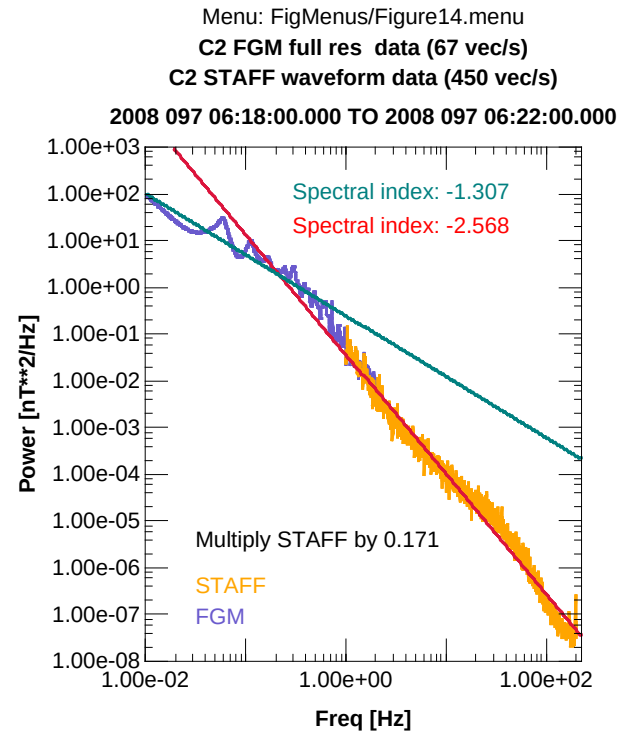


Figure 14. Spectra of the magnetic field power density from a time when the spacecraft were in the foreshock in Fig. 7. This can be compared to the spectra in Fig. 13.

of Sect. 4. If we use a relaxed definition, requiring only the presence of a definite tongue that extends beyond the nominal position of the core/halo, the number of diffusion observations increases to more than 18% (25% if we do not include events that are all foreshock).

There are only two sources of electrons from which the tongue and proto-halo can form: the strahl and the core/halo, with the core/halo being the more likely source. That conclusion comes from two lines of evidence: first, in the top plot in Fig. 12 there is no break in the strahl toward higher or lower densities corresponding to the break in the full-density spectrum at the upper edge of diffusion zone. The indication is that the strahl contributes very little density to the diffusion components, which leaves only the core/halo. Second, note the similarity between the upper and lower full-density spectra. In the lower spectrum the break is the result of the inclusion of the core/halo populations in the density, while in the upper spectrum the break results from the inclusion of the components of the diffusion. Thus, we are led to the suggestion that the diffusion component in the upper spectrum is the remains of the core/halo eVDFs that originally populated these energies. These arguments all point to the upper-energy core/halo electrons as the source of the diffusion populations.

The general picture as we see it is that the diffusion begins with angular diffusion and possibly a minimal diffusion in energy of the upper-energy core/halo electrons. What drives

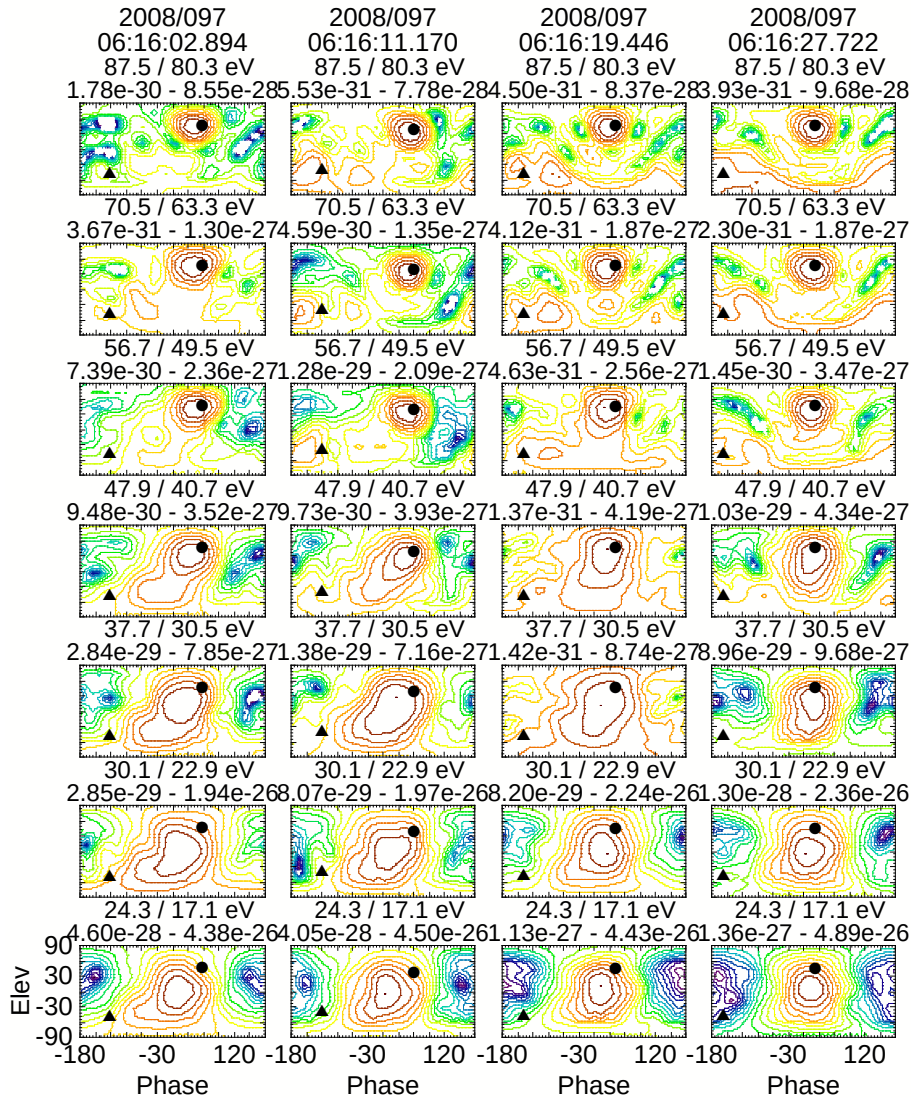


Figure 15. Set of four columns of ϕ - θ plots showing every other eVDF on a traversal from a region of diffusion (first two columns) into the foreshock (last two columns).

this is at the present unknown. The diffusion results in the creation of two populations of electrons within a confined energy range which we call the diffusion zone. There is currently no evidence that the strahl contributes to either population, but if it does, it is a minimal contribution. Within the upper energies of the diffusion range, there is no observed core/halo population. It is not inconceivable that at these energies the proto-halo represents the bulk of the core/halo population but shifted off the nominal core/halo radial flow location. The fluid flow in these energy steps is still primarily radial and not that different from what would be expected in the absence of diffusion.

One of the most puzzling observations is the total lack of observations of diffusion signatures anywhere inside the foreshock except in the immediate foreshock/solar wind in-

terface. The diffusion signatures, when present, do not penetrate more than 10 electron gyroradii into the foreshock. There is no expectation that the mechanisms responsible for the diffusion are active in the foreshock, but certainly diffusion created upstream of the foreshock should propagate into the foreshock in the same manner as the solar wind. Figure 15 shows the characteristics of every other eVDF during a transition from the pure solar wind with diffusion into the foreshock. The first two columns of plots are taken in the solar wind and exhibit diffusion characteristics: both a tongue of electrons and a proto-halo. By the third and fourth columns of the plots, the spacecraft has passed into the foreshock indicated by the presence of return electrons in the upper three energy plots. The existence of the proto-halo can be inferred from the extension of the core/halo due to the over-

lap of the two populations similar to that seen in the previous two columns of plots. In the last column, the eVDF exhibits pretty much the standard foreshock characteristics: strahl and return electrons at the upper energies and the core/halo at the lower energies.

The electrons within the diffusion zone are not in a stable configuration. External forces are required to create and maintain the drifts necessary to keep the proto-halo and tongue in the configuration they are observed to have in the diffusion zone. Turning off these forces will allow the diffusion populations to relax back into a stable configuration presumably close to what initially existed within the diffusion. The minimal penetration of the diffusion populations into the foreshock suggests that the plasma relaxes on a very short timescale back into or close to its pre-diffusion state. This would explain the absence of diffusion signatures interior to the foreshock/solar wind interface and may provide a look at how the diffusion alters the post-diffusion plasma populations.

6 Conclusions

The existence of a diffusion signature in the solar wind eVDF near 1 AU appears to be both common and significant. The diffusion manifests itself in the appearance of two new particle populations within a reasonably narrow energy range: the proto-halo and tongue. Both populations seem to be formed as a result of diffusion in the high-energy portion of the core/halo. Any contribution to their formation from the strahl appears to be minimal.

7 Data availability

With the exception of PEACE data, which were obtained from the Mullard Space Science Laboratory (MSSL) science data archive (http://www.mssl.ucl.ac.uk/missions/cluster/about_peace_data.php), all data were obtained from the Cluster Science Archive (CSA, <http://www.cosmos.esa.int/web/csa>).

Acknowledgements. The authors would like to acknowledge the work and role of the Cluster Science Archive (CSA) and thank the EFW and FGM teams for providing the data used in this study. We would also like to acknowledge the PEACE team at MSSL who worked on and are constantly improving the instrument calibration. Both of us would like to acknowledge support from NASA Grant NNX15AI88G.

The topical editor, M. Temmer, thanks three anonymous referees for help in evaluating this paper.

References

- Balogh, A., Dunlop, M. W., Cowley, S. W. H., Southwood, D. J., Thomlinson, J. G., Glassmeier, K. H., Musmann, G., Luhr, H., Buchert, S., Acuna, M. H., Fairfield, D. H., Slavin, J. A., Riedler, W., Schwingenschuh, K., and Kivelson, M. G.: The Cluster Magnetic Field Investigation, *Space Sci. Rev.*, 79, 65–91, doi:10.1023/A:1004970907748, 1997.
- Che, H. and Goldstein, M. L.: The Origin of Non-Maxwellian Solar Wind Electron Velocity Distribution Function: Connection to Nanoflares in the Solar Corona, *Astrophys. J. Lett.*, 795, L38, doi:10.1088/2041-8205/795/2/L38, 2014.
- Che, H., Goldstein, M. L., and Viñas, A. F.: Bidirectional energy cascades and the origin of kinetic Alfvénic and whistler turbulence in the solar wind., *Phys. Rev. Lett.*, 112, 061101, doi:10.1103/PhysRevLett.112.061101, 2014.
- Cornilleau-Wehrin, N., Chauveau, P., Louis, S., Meyer, A., Nappa, J. M., Perraut, S., Rezeau, L., Robert, P., Roux, A., de Villedary, C., de Conchy, Y., Friel, L., Harvey, C. C., Hubert, D., Lacombe, C., Manning, R., Wouters, F., Lefeuvre, F., Parrot, M., Pincon, J. L., Poirier, B., Kofman, W., and Louarn, P.: The Cluster Spatio-Temporal Analysis of Field Fluctuations (STAFF) Experiment, *Space Sci. Rev.*, 79, 107–136, doi:10.1023/A:1004979209565, 1997.
- Cornilleau-Wehrin, N., Mirioni, L., Robert, P., Bouzid, V., Maksimovic, M., de Conchy, Y., Harvey, C. C., and Santolík, O.: STAFF Instrument Products Distributed Through the Cluster Active Archive, in: *The Cluster Active Archive, Studying the Earth's Space Plasma Environment*, edited by: Laakso, H., Taylor, M. G. T. T., and Escoubet, C. P., *Proceedings of Astrophysics and Space Science*, Springer, Berlin, 11, 159–168, doi:10.1007/978-90-481-3499-1_10, 2010.
- Dum, C. T., Marsch, E., and Pilipp, W.: Determination of wave growth from measured distribution functions and transport theory, *J. Plasma Phys.*, 23, 91–113, doi:10.1017/S0022377800022170, 1980.
- Fazakerley, A. N., Lahiff, A. D., Wilson, R. J., Rozum, I., Anekallu, C., West, M., and Bacai, H.: PEACE Data in the Cluster Active Archive, in: *The Cluster Active Archive, Studying the Earth's Space Plasma Environment*, edited by: Laakso, H., Taylor, M. G. T. T., and Escoubet, C. P., *Proceedings of Astrophysics and Space Science*, Springer, Berlin, 11, 129–144, doi:10.1007/978-90-481-3499-1_8, 2010.
- Feldman, W. C., Asbridge, J. R., Bame, S. J., Montgomery, M. D., and Gary, S. P.: Solar wind electrons, *J. Geophys. Res.*, 80, 4181–4196, 1975.
- Gary, S. P. and Saito, S.: Broadening of solar wind strahl pitch-angles by the electron/electron instability: Particle-in-cell simulations, *Geophys. Res. Lett.*, 34, L14111, doi:10.1029/2007GL030039, 2007.
- Gary, S. P., Saito, S., and Li, H.: Cascade of whistler turbulence: Particle-in-cell simulations, *Geophys. Res. Lett.*, 35, L02104, doi:10.1029/2007GL032327, 2008.
- Gloag, J. M., Lucek, E. A., Alconcel, L.-N., Balogh, A., Brown, P., Carr, C. M., Dunford, C. N., Oddy, T., and Soucek, J.: FGM Data Products in the CAA, in: *The Cluster Active Archive, Studying the Earth's Space Plasma Environment*, edited by: Laakso, H., Taylor, M. G. T. T., and Escoubet, C. P., *Proceedings of Astrophysics and Space Science*, Springer, Berlin, 11, 109–128, doi:10.1007/978-90-481-3499-1_7, 2010.

- Gurgiolo, C., Goldstein, M. L., Viñas, A. F., and Fazakerley, A. N.: Direct observations of the formation of the solar wind halo from the strahl, *Ann. Geophys.*, 30, 163–175, doi:10.5194/angeo-30-163-2012, 2012.
- Gustafsson, G., Bostrom, R., Holback, B., Holmgren, G., Lundgren, A., Stasiewicz, K., Ahlen, L., Mozer, F. S., Pankow, D., Harvey, P., Berg, P., Ulrich, R., Pedersen, A., Schmidt, R., Butler, A., Fransen, A. W. C., Klinge, D., Thomsen, M., Falthammar, C.-G., Lindqvist, P.-A., Christenson, S., Holtet, J., Lybekk, B., Sten, T. A., Tanskanen, P., Lappalainen, K., and Wygant, J.: The Electric Field and Wave Experiment for the Cluster Mission, *Space Sci. Rev.*, 79, 137–156, doi:10.1023/A:1004975108657, 1997.
- Hammond, C. M., Feldman, W. C., McComas, D. J., and Forsyth, R. J.: Variation of electron-strahl width in the high-speed solar wind: ULYSSES observations, *Astron. Astrophys.*, 316, 350–354, 1996.
- Johnstone, A. D., Alsop, C., Gurge, S., Carter, P. J., Coates, A. J., Coker, A. J., Fazakerley, A. N., Grande, M., Gowen, R. A., Gurgiolo, C., Hancock, B. K., Narheim, B., Preece, A., Sheather, P. H., Winningham, J. D., and Woodcliffe, R. D.: PEACE: A plasma electron and current experiment, *Space Sci. Rev.*, 79, 351–398, 1997.
- Khotyaintsev, Y., Lindqvist, P.-A., Eriksson, A., and André, M.: The EFW Data in the CAA, in: *The Cluster Active Archive, Studying the Earth's Space Plasma Environment*, edited by: Laakso, H., Taylor, M. G. T. T., and Escoubet, C. P., *Proceedings of Astrophysics and Space Science*, Springer, Berlin, 11, 97–108, doi:10.1007/978-90-481-3499-1_6, 2010.
- Landi, S., Matteini, L., and Pantellini, F.: On the Competition Between Radial Expansion and Coulomb Collisions in Shaping the Electron Velocity Distribution Function: Kinetic Simulations, *Astrophys. J. Lett.*, 760, 143, doi:10.1088/0004-637X/760/2/143, 2012.
- Larson, D. E., Lin, R. P., McFadden, J. P., Ergun, R. E., Carlson, C. W., Anderson, K. A., Phan, T. D., McCarthy, M. P., Parks, G. K., Rème, H., Bosqued, J. M., d'Uston, C., Sanderson, T. R., Wenzel, K. P., and Lepping, R. P.: Probing the Earth's bow shock with upstream electrons, *Geophys. Res. Lett.*, 23, 2203–2206, doi:10.1029/96GL02382, 1996.
- Lin, R. P.: Wind observations of suprathermal electrons in the interplanetary medium, *Space Sci. Rev.*, 86, 61–78, 1998.
- Maksimovic, M., Zouganelis, I., Chaufray, J.-Y., Issautier, K., Scime, E. E., Littleton, J. E., Marsch, E., McComas, D. J., Salem, C., Lin, R. P., and Elliott, H.: Radial evolution of the electron distribution functions in the fast solar wind between 0.3 and 1.5 AU, *J. Geophys. Res.-Space*, 110, 9104, doi:10.1029/2005JA011119, 2005.
- Owens, M. J., Crooker, N. U., and Schwadron, N. A.: Suprathermal electron evolution in a Parker spiral magnetic field, *J. Geophys. Res.*, 113, A11104, doi:10.1029/2008JA013294, 2008.
- Pavan, J., Viñas, A. F., Yoon, P. H., Ziebell, L. F., and Gaelzer, R.: Solar Wind Strahl Broadening by Self-generated Plasma Waves, *Astrophys. J. Lett.*, 769, L30, doi:10.1088/2041-8205/769/2/L30, 2013.
- Pierrard, V., Lazar, M., and Schlickeiser, R.: Evolution of the electric distribution function in whistler wave turbulence of the solar wind, *Sol. Phys.*, 269, 421–438, doi:10.1007/s11207-010-9700-7, 2011.
- Pilipp, W. G., Miggenrieder, H., Montgomery, M. D., Mühlhäuser, K. H., Rosenbauer, H., and Schwenn, R.: Characteristics of electron velocity distribution functions in the solar wind derived from Helios Plasma Experiment, *J. Geophys. Res.*, 92, 1075–1092, 1987a.
- Pilipp, W. G., Miggenrieder, H., Mühlhäuser, K. H., Rosenbauer, H., Schwenn, R., and Neubauer, F. M.: Variations of electron velocity distribution functions in the solar wind, *J. Geophys. Res.*, 92, 1103–1118, 1987b.
- Rosenbauer, H., Miggenrieder, H., Montgomery, M. D., and Schwenn, R.: Preliminary results of the Helios plasma experiment, in: *Physics of Solar Planetary Environments*, edited by: Williams, D. J., American Geophysical Union, Washington DC, USA, p. 319, 1976.
- Rosenbauer, H., Schwenn, R., Marsch, E., Meyer, B., H. M., Montgomery, M. D., Mühlhäuser, K. H., Pilipp, W., Voges, W., and Zink, S. M.: A survey on initial results of the Helios plasma experiment, *J. Geophys.*, 42, 561–580, 1977.
- Saito, S. and Gary, S. P.: Whistler scattering of suprathermal electrons in the solar wind: Particle-in-cell simulations, *J. Geophys. Res.*, 112, A06116, doi:10.1029/2006JA012216, 2007a.
- Saito, S. and Gary, S. P.: All whistlers are not created equally: Scattering of strahl electrons in the solar wind via particle-in-cell simulations, *Geophys. Res. Lett.*, 34, L01102, doi:10.1029/2006GL028173, 2007b.
- Seough, J., Nariyuki, Y., Yoon, P. H., and Saito, S.: Strahl Formation in the Solar Wind Electrons via Whistler Instability, *Astrophys. J. Lett.*, 811, L7, doi:10.1088/2041-8205/811/1/L7, 2015.
- Stverák, v. S. v., Maksimovic, M., Trávníček, P., Marsch, E., Fazakerley, A. N., and Scime, E. E.: Radial evolution of nonthermal electron populations in the low-latitude solar wind: Cluster and Ulysses observations, *J. Geophys. Res.*, 114, A05104, doi:10.1029/2008JA013883, 2009.
- Viñas, A. F. and Gurgiolo, C.: Spherical harmonic analysis of particle velocity distribution function: Comparison of moments and anisotropies using Cluster data, *J. Geophys. Res.*, 114, A01105, doi:10.1029/2008JA013633, 2009.
- Viñas, A. F., Gurgiolo, C., Nieves-Chinchilla, T., Gary, S. P., and Goldstein, M. L.: Whistler waves driven by anisotropic 3D strahl velocity distributions in the solar wind: Cluster observations, in: *AIP Proceedings of Solar Wind 12 Conference*, edited by: Maksimovic, M., Issautier, K., Meyer-Vernet, N., Moncuquet, M., and Pantellini, F., American Institute of Physics, New York, NY, USA, p. 265, 2010.
- Vocks, C.: Kinetic Models for Whistler Wave Scattering of Electrons in the Solar Corona and Wind, *Space Sci. Rev.*, 172, 303–314, doi:10.1007/s11214-011-9749-0, 2012.
- Vocks, C., Lin, R. P., and Mann, G.: Electron halo and strahl formation in the solar wind by resonant interaction with whistler waves, *Astrophys. J.*, 627, 540–549, doi:10.1086/430119, 2005.
- Vocks, C., Mann, G., and Rausche, G.: Formation of suprathermal electron distributions in the quiet solar corona, *Astron. Astrophys.*, 480, 527–536, doi:10.1051/0004-6361:20078826, 2008.
- Wang, L., Lin, R. P., Salem, C., Pulupa, M., Larson, D. E., Yoon, P. H., and Luhmann, J. G.: Quiet-time Interplanetary 2–20 keV Superhalo Electrons at Solar Minimum, *Astrophys. J. Lett.*, 753, L23, doi:10.1088/2041-8205/753/1/L23, 2012.